Red Shift of CT-Band in Cubic Y₂O₃:Eu³⁺ upon Increasing the Eu³⁺ Concentration

Daniel den Engelsen, Terry G. Ireland,ᶻ Rupinder Dhillon, George Fern,* Paul G. Harris, and Jack Silver*

Centre for Phosphor and Display Materials, Wolfson Centre for Materials Processing, Brunel University London, Uxbridge, Middlesex UB8 3PH, United Kingdom

In this article we describe the redshift of the charge transfer band of nanosized cubic $(Y_{1-x}Eu_x)_2O_3$ upon increasing the Eu^{3+} concentration. This redshift amounts to 0.43 eV (25 nm) in going from 0.1 Mol % Eu^{3+} to 100 Mol % (which is pure Eu_2O_3). The charge transfer band consists of two broad sub-bands; both shift almost parallel with the Eu^{3+} concentration and are related to the two symmetry sites for the cation, C_2 and C_{3i}, in the bixbyite-type lattice. The area ratio of the bands is 3:1 and is the first direct evidence for the population of the two lattice sites by the Eu^{3+} cations being in accord with the crystal structure ratio. A model is presented that quantitatively describes the redshift of the charge transfer band of $(Y_{1-x}Eu_x)_2O_3$. This model is based on the Madelung energy of the transferred charge. Other models are briefly discussed, but are discarded.

The red luminescent phosphor Y₂O₃:Eu³⁺ has been studied extensively, because of its rather high efficiency and high stability to electron bombardment, UV-irradiation and ion bombardment. These attributes led cubic Y₂O₃:Eu³⁺ to be widely employed in cathode ray tubes (projection tubes) and it is still used in fluorescent lamps. Many properties of this phosphor have been studied by photoluminescence (PL) and cathodoluminescence (CL) spectrometry and have been well documented, because of its industrial applications. Notwithstanding the extensive literature on Y₂O₃:Eu³⁺, voids still exist in our knowledge on this phosphor. One of these voids is related to the position of the charge transfer (CT) band in the excitation spectrum, although this subject has been widely studied. In the present study we shall focus on the position of the CT-band, which is located at 253 nm in Y₂O₃ when doped with 0.1 Mol % Eu³⁺.[1] The wavelength of the maximum of the CT-band in Y₂O₃:Eu³⁺, indicated by the E^{CT} in this study and expressed in nanometers (nm) or electron-volts (eV) depends on the concentration of the Eu³⁺ dopant and the size of the phosphor particles.[2–10] Upon increasing the Eu³⁺ concentration between 1 and 15 Mol % a redshift of the E^{CT} of about 6 nm has been observed,[2–4] whereas Kang et al.[5] did not observe a change of E^{CT} in increasing the Eu³⁺ dope from 2 to 10 Mol %. Some peculiar observations were reported on the effect of the particle size of Y₂O₃:Eu³⁺. Igarashi et al.[6] reported a blueshift of the E^{CT} of 6 nm in reducing the particle size from 2.1 μm to 56 nm; Fu et al.[7] measured a blueshift of 5 nm in reducing the particle size from 2.1 μm down to 10 nm. The opposite trend was found by others. Jia et al.[8] measured a redshift of the E^{CT} of 6 nm upon particle size reduction from 2–3 μm to 7 nm. Shang et al.[9] and Zhang et al.[10] reported large red shifts, 11 nm and 7 nm, in reducing the size of Y₂O₃:Eu³⁺ nanoparticles from 40 nm to 9 nm and from 40 nm to 5 nm respectively. Semiconductor particles are expected to show a blueshift of their absorption peaks in reducing the particle size from 15 to 5 nm because of quantum confinement.[11] The observed opposite trend indicates that quantum confinement cannot explain the reported phenomena in nanosized Y₂O₃:Eu³⁺.

The E^{CT} of Eu³⁺ doped phosphors with different host lattices has been widely studied.[12–19] Blasse[12] suggested that the electrostatic potential at the O²⁻ ligand is largely determining the energy of the CT-band, whereas Hoefdraad[13] indicated that the E^{CT} in some classes of phosphors may be described with Jørgensen's concept of optical electronegativity χ:[14]

$$E^{CT} = 3.72[\chi(O^{2-}) - \chi(M^{3+})], \quad [1]$$

where $\chi(O^{2-})$ is the optical electronegativity of the O²⁻ ion, and $\chi(M^{3+})$ is the optical electronegativity of the central metal ion, Y³⁺ or Eu³⁺ in our case. The constant 3.72 in Eq. 1 adapts electronegativity to the eV-scale. When we set $\chi(O^{2-}) = 3.44$ (Pauling's electronegativity), we find for $\chi(Eu^{3+}) = 2.12$, which is larger than 1.2 in Pauling's scale. In spite of this discrepancy, it is possible to represent the E^{CT} of various classes of phosphors with Eq. 1.[13,15–17] Dorenbos[17] pointed out that Eq. 1 necessarily has a limited scope, because it does not account for the site size and the binding strength of the valence band electrons. Krumpel et al.[18] have proposed a correction to Eq. 1 that accounts for size variations of the site, where the Eu³⁺ dopant is located. This enabled the comparison between the E^{CT} values of similar phosphors doped with Eu³⁺ in terms of electronegativity.

The E^{CT} and the bandgap Eg of phosphors like Y₂O₃:Eu³⁺ are related by the photo-ionization (or photoconductivity) threshold E_{PI} according:[19]

$$E_g = E^{CT} + E_{PI}. \quad [2]$$

If E_{PI} is not being affected strongly by changing the dopant concentration, then a plot of Eg versus Eu-concentration would give information on the E^{CT}. The bandgap of Y₂O₃:Eu³⁺ with Eu³⁺ concentrations between 1 and 11 Mol % has recently been evaluated by Prasanna kumar et al.[20] They found that the Eg decreased from 5.3 eV at 1% Eu³⁺ to 4.1 eV at 11 Mol % Eu³⁺, which is a big change over a limited concentration range. It is unknown whether the E_{PI} is also changing over this concentration range; hence, it is impossible to relate this bandgap information to E^{CT}.

Apart from the position of the CT-band of Y₂O₃:Eu³⁺, one may also consider its composition in terms of C_2 and C_{3i} contributions, in a similar way as we have done in our treatment of the $^7F_6 \rightarrow {}^9D_J$ excitation band in Y₂O₃:Tb³⁺.[21] By deconvolution two separate bands have been found: a C_2-related band at 282 nm and a C_{3i}-related band at 305 nm. Jia et al.[7] found that the CT-band in Y₂O₃:Eu³⁺ has contributions from Eu³⁺ at a C_2-site and a C_{3i}-site. They concluded that Eu³⁺ in C_{3i}-sites contributed most to the CT-band and that this C_{3i} contribution is mainly at the VUV-side of the CT-band.

The theories mentioned above on the change of the E^{CT} in Y₂O₃:Eu³⁺ are based on the following observations:

1. Redshift of the E^{CT} when the Eu³⁺ concentration is increased in Y₂O₃:Eu³⁺;
2. Redshift of the E^{CT} when the diameter of Y₂O₃:Eu³⁺ nanoparticles is decreased;
3. Variation of the E^{CT} in similar phosphors doped with Eu³⁺.

**Electrochemical Society Member.
ᶻE-mail: terry.ireland@brunel.ac.uk

Since the studies of Pelova et al.,[2] Chang et al.[3] and Hang et al.[4] refer to a limited range of Eu^{3+} concentrations, we thought it worthwhile to extend the range between 0.001 and 1 of x in $(Y_{1-x}Eu_x)_2O_3$. In this systematic study of $(Y_{1-x}Eu_x)_2O_3$ we measured and analyzed beside the E^{CT} also the intensity ratios of some peaks in the excitation and emission spectra.

Experimental

Synthesis of $(Y_{1-x}Eu_x)_2O_3$ - Synthesis of $(Y_{1-x}Eu_x)_2O_3$ – The following chemicals were used in this work, yttrium oxide (99.99%) and europium oxide (99.99%) (Ampere Industrie, France); urea, nitric acid and isopropanol (IPA) (Fisher Scientific, UK); all chemicals were used as received. The synthesis of Y_2O_3:Eu^{3+} nanoparticles by the homogeneous hydrothermal decomposition of urea method which has been extensively described in our earlier work.[21–25] The ageing of the turbid suspensions after the onset of precipitation was continued for one hour at a temperature above 85°C (this is the temperature at which urea slowly decomposes in aqueous media at a rate that is sufficient to supply the reactants in a controlled manner by a single nucleation event followed by uniform particle growth of the desired precipitate). After this ageing period the precipitate was filtered, washed three times with de-ionized water and dried in an oven at 80°C. The phosphor precursor particles were then annealed at 980°C in a furnace in air for four hours to yield cubic nanosized Y_2O_3:Eu^{3+} phosphor particles. This annealing temperature favors the creation of cubic crystallites that yielded optimum luminescence characteristics.[23] The crystal structure of the $(Y_{1-x}Eu_x)_2O_3$ samples after annealing was bixbyite, which is cubic with some O^{2-} vacancies.[20–23] The $(Y_{1-x}Eu_x)_2O_3$ samples that were synthesized had Eu^{3+} concentrations of 0.1, 0.3, 1, 2, 4, 5, 6, 8, 10, 15, 20, 25, 30, 40, 50, 60, 70, 80, 90 and 100 Mol %.

Equipment and methods.—Photoluminescence (PL) spectra (both excitation and emission) of the samples were collected using a Bentham phosphor spectrometer system (Bentham Instruments Ltd., Reading, UK.), configured with M300 excitation and emission monochromators and 0.2 mm slits. High resolution spectra and various excitation spectra at wavelengths in the range between 220 and 500 nm were recorded with a Horiba Jobin Yvon Fluorolog-3 spectrofluorometer (Edison, USA). The absolute wavelength calibration of the monochromators could be off by maximally 1 nm; however, relative wavelength values were accurate within 0.05 nm.

The morphology and particle size assessment of the phosphor powders were conducted in a FESEM, Supra 35 VP, Carl Zeiss, Germany.

Results and Discussion

Figs. 1a–1c show FESEM images of annealed $(Y_{1-x}Eu_x)_2O_3$ spherical phosphor particles on a carbon substrate. From Figs. 1a to 1c it can be derived that the average diameter of the particles varied between 200 and 250 nm, which did not depend on the concentration of Eu^{3+}: it was virtually equal for all concentrations. All the samples of $(Y_{1-x}Eu_x)_2O_3$ spherical phosphor particles were observed to be comprized of tessellated crystallites 40 nm to 100 nm; some particles indicate that there are small voids within.

Fig. 2 shows the excitation spectra of $(Y_{1-x}Eu_x)_2O_3$ with x = 0.02, 0.04, 0.05, 0.06, 0.15, 0.2, 0.4, 0.6, 0.7 and 1.0 between 250 and 500 nm, monitored at 611.8 nm. This 611.8 nm line in the emission spectrum of Y_2O_3:Eu^{3+} determines the red fluorescence of the phosphor; it has been assigned to the $^5D_0$ - $^7F_2$ (C_2) transition of Eu^{3+} at a C_2 lattice site.[1,26]

Fig. 2 shows that the E^{CT} exhibits a substantial redshift of 22 nm in going from 2% to 100% Eu^{3+}, while the 4f→4f transitions at 305 nm ($^7F_0$ - $^5F_2$), 467 nm ($^7F_0$ - $^5D_2$) and the other transitions in between are not changing. The spectrum of Eu_2O_3 (100% spectrum) is apart from a shift of the CT-band not essentially different from the spectra of $(Y_{1-x}Eu_x)_2O_3$ with x < 1. This result is different from the excitation spectrum of Eu_2O_3 published by Ozawa in 1966.[27] In Fig. 2 the intensity of the $^7F_0$ - $^5L_6$ transition for pure Eu_2O_3 is a little bit

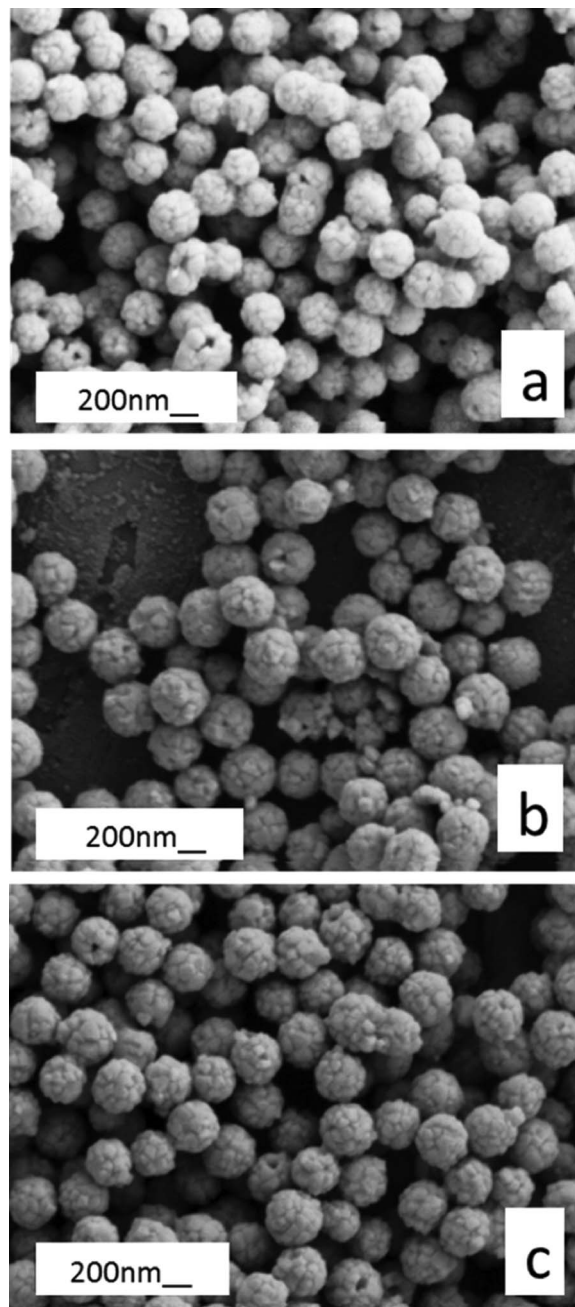**Figure 1.** FESEM images of Y_2O_3:Eu^{3+} at 5 kV. (a) 1% Eu^{3+}, (b) 50% Eu^{3+} and (c) 100% Eu^{3+}.

smaller than the intensity of the CT-band at 285 nm, whereas Ozawa found that the intensity of the $^7F_0$ - $^5L_6$ transition is almost 3 times larger.

The CT-bands in Fig. 2 are rather broad and show a tail at the low wavelength side although this cannot be observed easily in all the spectra presented in Fig. 2. This asymmetry could indicate the presence of more absorption bands. Therefore, the structure of the CT-band was analyzed with a deconvolution technique using four symmetric Gaussian profiles in the wavelength range between 250 and 315 nm: this allows the small peak at 289 nm and the $^7F_0$→$^5F_2$ transition at 302 nm to be included, because at high Eu^{3+} concentration the CT-band is engulfing the small peak at 289 nm. The main advantage of this procedure was that the E^{CT} could be determined in a consistent way, instead of deriving it from a curve fitting procedure around the maximum that did not account for the small peak at 289 nm. In
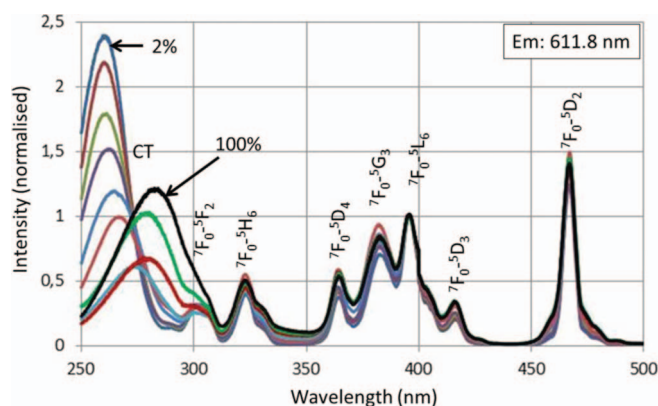
Figure 2. Excitation spectra of $(Y_{1-x}Eu_x)_2O_3$ with various Eu^{3+} concentrations recorded with Bentham spectrometer. Spectra have been normalized to unity for the $^7F_0 \rightarrow {}^5L_6$ transition at 395.8 nm. Spectra for Eu^{3+} concentrations of 2 Mol % and 100 Mol % are indicated. The 40% and 60% Eu^{3+} spectra yielded the lowest CT intensity.

our previous work the deconvolution method with Gaussian profiles has been reported;[21–23] therefore, we may suffice by showing the results. In Fig. 3 deconvolutions are represented at low and high Eu^{3+} concentrations using an eV (energy) scale.

The four Gaussian profiles shown in Figs. 3a and 3b were fitted to the experimental spectrum using a least squares algorithm with Microsoft's Excel solver. It is important to realize that Fig. 3 shows the CT band plotted on an energy scale so the high energy side corresponds to the low wavelength side of Fig. 2. Thus in Fig. 3 the tail (seen at low wavelength in Fig. 2) is apparent at high energy in Figure 3. Fig. 3a shows that CT-1 for $(Y_{0.9}Eu_{0.1})_2O_3$, has its maximum height
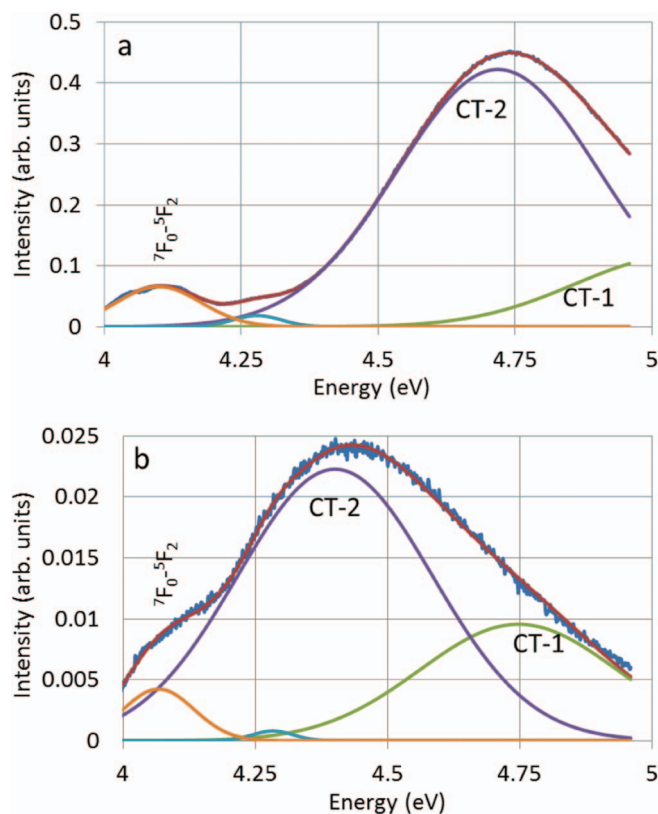

Figure 3. Deconvolution of CT-band of $(Y_{1-x}Eu_x)_2O_3$ with x = 0.1 (a) and x = 0.8, (b) CT-1 is the high energy sub-band of the CT-band and CT-2 is the low energy sub-band. The small peak at 289 nm in Fig. 2 can be noticed at 4.28 eV.
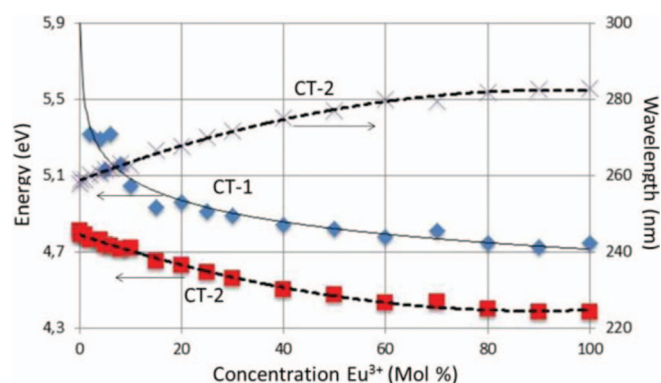

Figure 4. E^{CT} versus Eu^{3+} concentration. Left vertical axis is the eV-scale, right vertical axis is the wavelength scale. For reasons of clarity the CT-1 curve (nm-scale) has been omitted. The curves are polynomials fitted to the experimental points.

at E > 4.96 eV (or λ < 250 nm), being beyond the limit of the Bentham spectrometer. At low Eu^{3+} concentrations some spectra were also recorded with the Fluorolog-3 to verify the trend between 235 nm and 250 nm: at 235 nm the absorption of the CT-band was low. Nevertheless, for the low concentrations of Eu^{3+} the determination of the CT-1 band was less reliable; however, at Eu^{3+} concentrations larger than 15 Mol % Eu^{3+}, deconvolution yielded satisfactory results, because of the large number of data points: 642 points for the represented energy range in Figs 3a and 3b. These Figs. also show that CT-2 is 2 to 3 times larger than CT-1 while their band widths are almost identical. Although the vertical scales in Figs. 3a and 3b are in arbitrary units, the signal for the sample with 80% Eu^{3+} was much weaker due to concentration quenching. This is reflected in the increased noisiness of the spectrum in Fig. 3b.

Fig. 4 shows a plot of the E^{CT} versus the concentration of Eu^{3+} in $Y_2O_3:Eu^{3+}$. The curves for CT-1 and CT-2 in Fig. 4, which have been fitted to the experimental points, are more or less parallel between 20 and 100 Mol % Eu^{3+}. From the CT-2 curves it can be derived that the redshift from 0.1 to 100 Mol % Eu^{3+} is −0.43 eV or 25 nm. The curves also indicate that at high Eu^{3+} concentrations the redshift is levelling off.

Chang et al.[3] showed that the E^{CT} for 40 nm $Y_2O_3:Eu^{3+}$ crystallites increased from about 254 nm to about 259 nm upon increasing the Eu^{3+} concentration from 3 to 14 Mol %: their E^{CT} are slightly lower than the E^{CT-2} in Figure 4 at those Eu^{3+} concentrations. It should be mentioned that the data of Chang et al.[3] refer to non-deconvoluted spectra: the E^{CT} was extracted from the graph in their publication. By deconvolution, the values of E^{CT-2} shift by 2–3 nm to larger wavelengths compared to the (non-deconvoluted) over-all maximum of the CT-band, as can be derived from Figs. 3a and 3b. The E^{CT}-data of Pelova et al.,[2] which refer to $Y_2O_3:Eu^{3+}$ (1 and 3 Mol % Eu^{3+}) with non-defined particle and crystallite size, are about 10 nm lower than the values of Chang et al.[3] Hang et al.[4] have recently reported a redshift of 7 nm from 248 nm at 1 Mol % Eu^{3+} to 255 nm at 15 Mol %. Although they also found a second Gaussian profile at the high energy side of the CT-band, the absorption of this second band is low and deconvolution has almost no effect on the E^{CT}. As already mentioned in the introduction, Kang et al.[5] did not find a change of the E^{CT} upon increasing the Eu^{3+} concentration from 2 to 10 Mol %. From the excitation spectrum of pure Eu_2O_3 published by Ozawa[26] it is impossible to derive a value for E^{CT}. The published E^{CT} for $Y_2O_3:Eu^{3+}$ particles in the range between 40 nm and 2–5 μm having Eu^{3+} dopes ≤3 Mol % vary between 239 nm and 262 nm;[2–10] this variation is surprisingly large. Since these measurements of the excitation spectra were carried out by different groups on $Y_2O_3:Eu^{3+}$ that was synthesized by different technologies, we assume that the synthesis methods and annealing technologies are responsible for this large spread of the E^{CT}. The published wavelengths of the emission lines of $Y_2O_3:Eu^{3+}$ show
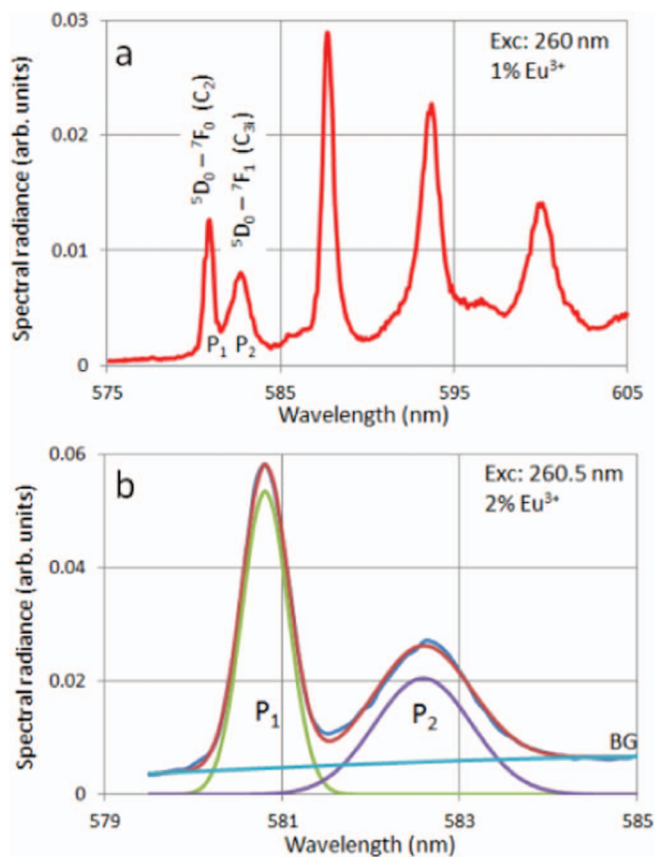
Figure 6. Ratio of the radiances of P_1 and P_2 versus Eu^{3+} concentration in Y_2O_3:Eu^{3+}.

Figure 5. Part of PL spectrum. $^5D_0 \rightarrow {}^7F_0$ (C_2) transition at 580.6 nm is indicated by P_1, the $^5D_0 \rightarrow {}^7F_1$ (C_{3i}) transition at 582.4 nm is indicated by P_2. (a) $(Y_{0.99}Eu_{0.01})_2O_3$ excited at 260 nm, (b) Deconvolution example with two Gaussian profiles and background correction (BG) for $(Y_{0.99}Eu_{0.01})_2O_3$ excited at 260.5 nm.

a much smaller spread; this spread is assumed to be mainly caused by small calibration errors of the spectrometers of about 1 nm. Since we have synthesized and annealed all samples in exactly the same way leading to identical particle size and surface morphology as shown in Figure 1, it is assumed that we have ruled out the afore mentioned source of spread: in other words, the observed redshift of the E^{CT} is an intrinsic property of $(Y_{1-x}Eu_x)_2O_3$ upon increasing x.

Fig. 5a shows the PL-spectrum of $(Y_{0.99}Eu_{0.01})_2O_3$ between 575 nm and 605 nm. The $^5D_0 \rightarrow {}^7F_1$ (C_{3i}) transition at 582.4 nm is one of the few well-separated C_{3i} transitions in the emission spectrum of Y_2O_3:Eu^{3+}: it is therefore a hallmark for detailed studies on the energy flow in this phosphor.[4,22,28–30] As an indicator for the energy flow we take the ratio of the radiances of P_1 and P_2, being the $^5D_0 \rightarrow {}^7F_0$ (C_2) transition at 580.6 nm and the $^5D_0 \rightarrow {}^7F_1$ (C_{3i}) transition at 582.4 nm respectively. Radiance is a better criterion in the case of a difference between the full widths at half maximum (FWHM). Figs. 5a and 5b show a clear difference between the FWHM of P_1 and P_2. This difference cannot be observed at low temperatures of 4 K[26] and 77 K.[30] Since there are no other interfering transitions in the wavelength range between 579 and 584 nm,[28] we assume that the C_{3i} peak at 582.4 nm experiences more vibronic broadening at room temperature than the neighboring C_2 at 580.6 nm.

The determination of the radiances requires a profile representation of the peaks; we took Gaussian profiles and applied also a background correction as indicated in Fig. 5b. The radiances of P_1 and P_2 were calculated with a formula that was presented in our earlier work.[31] The result is represented in Fig. 6, in which the ratio of the radiances of P_1 and P_2 has been plotted versus the Eu^{3+} concentration. Fig. 6 does not show the whole concentration range of our experiments. The reason is
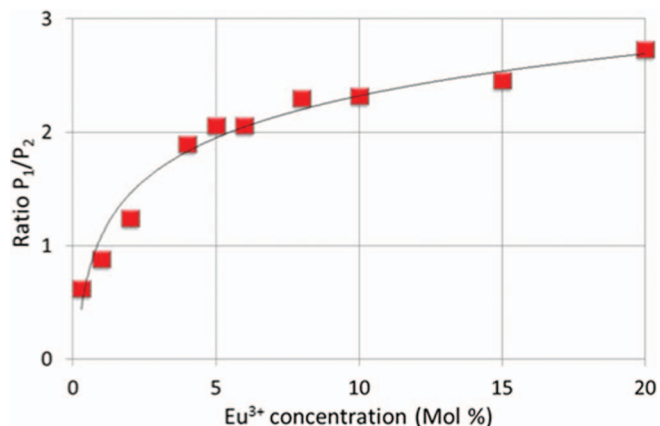
that at Eu^{3+} concentrations larger than 20 Mol % the noisiness of the spectra increased and the determination of the radiance of P_2 became less accurate. Nevertheless, the trend at low Eu^{3+} concentration agrees with the CL results described in our publication.[22] It indicates that energy from Eu^{3+} at a C_{3i} site is being transported to Eu^{3+} at a C_2 site when the distance between the Eu^{3+} in the lattice decreases.

Jia et al.[7] claimed that the CT-band in Y_2O_3:Eu^{3+} consists of two separate bands, which they assigned to the C_2 and C_{3i} sites of Eu^{3+} ions in the Y_2O_3 host; however, the shape and position of their bands differ substantially from the results presented in Figs. 3a and 3b. We have also analyzed our data in more detail and the results are shown in Fig. 7, which is a plot of the ratio of the radiances of CT-2 and CT-1 versus the Eu^{3+} concentration (in Mol %). The radiances of CT-2 and CT-1, having Gaussian profiles, are calculated from the fitted amplitude and width parameter. It can be seen that the CT-1 and CT-2 bands are in a ratio of 1:3, which coincides with the ratio of the C_{3i} and C_2 lattice sites: so we could infer that what we see in the deconvolution of the CT band is evidence for the fact that both Eu^{3+} sites make different contributions to the CT band as might be expected. The fact that we assign the bands in the opposite sense to Jia et al.[7] may be because their nanoparticles are very small and though they claim they also show bulk, their spectra do not prove this and their annealed nanoparticles may not have coalesced: they may only have partially sintered. Indeed we have previously shown that annealing nanoparticles does not lead to rapid growth even in time periods of 24 hours or more (unfortunately, Jia et al.[7] do not give
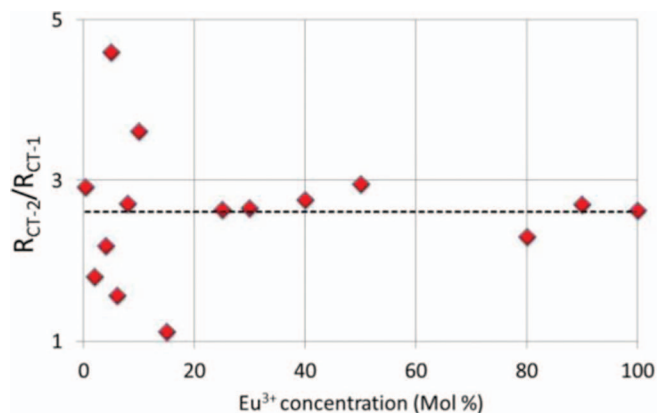

Figure 7. Ratio of radiance of CT-2 and CT-1 versus the Eu^{3+} concentration. The radiance of a band is the integrated spectral radiance. The dashed line represents the best fit through the experimental points. At low Eu^{3+} concentration the radiance of CT-1 cannot be determined accurately from our spectra.
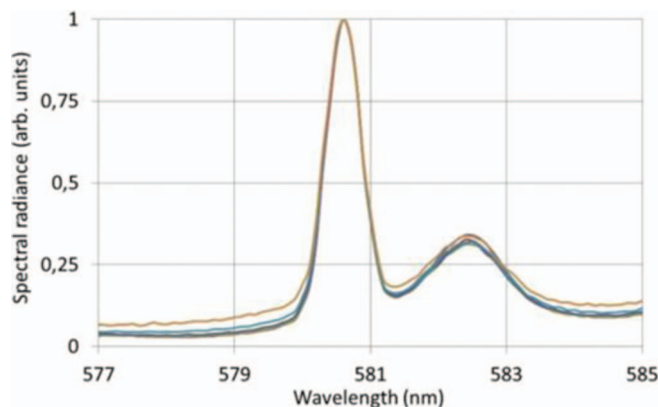
Figure 8. Overlay of spectra of 4% Y_2O_3:Eu^{3+}, excited at 250 nm, 255 nm, 260 nm, 265 nm, 270 nm and 275 nm. Normalized to unity at 580.6 nm.

their annealing time). The fact that the ratio we observe is so close to 1:3 is good evidence for our homogenous precipitation method giving atomic mixing, and is to our knowledge the best evidence to date for the distribution of the Eu^{3+} cations being in accord with the known crystal structure with no evidence for a site preference. In this Figure is a plot showing these results, it is important to note that the samples with less than 20% Eu^{3+} cations have spectra that are beyond the range of our spectrometers at the low wavelength end so fitting the edge of the spectra is suspect.

In the light of this assignment we have investigated the nature of the CT-1 and CT-2 bands by recording PL spectra in the range between 570 nm and 590 nm as a function of the excitation wavelength. If CT-1 would be related to Eu^{3+} at a C_{3i}-lattice site and CT-2 to the Eu^{3+} at a C_2-lattice site, then it might be expected that the ratio between the peaks P_1 and P_2 in Fig. 5 would vary, because P_1 is a C_2-transition and P_2 is a C_{3i}-transition.

Fig. 8 is an overlay of spectra of 4% Y_2O_3:Eu^{3+} excited at 250 nm, 255 nm, 260 nm, 265 nm, 270 nm and 275 nm. It can be seen that the ratio between these peaks does not change by varying the excitation wavelength. Similar results were obtained for Y_2O_3:Eu^{3+} with other concentrations and also for Eu_2O_3 an overlay-graph was obtained that was essentially identical to Fig. 8. From these results it might be concluded that CT-1 and CT-2 do not have symmetry-related characteristics, however it is possible that putting energy into the CT band at any wavelength could lead to a redistribution of this energy over the entire lattice as this is a band that is lattice dependent: hence, it would then not lead to symmetry related emission. Of course then, this negative finding does not contradict the assignment we have made for the nature of CT-1 and CT-2. We already noticed the parallel behavior of the CT-1 and CT-2 curves in Fig. 4. Dorenbos[16] mentioned that the FWHM of the CT-band of Eu^{3+} in many host lattices is between 0.6 and 1.2 eV: CT-2 and CT-1 together yield an FWHM of about 0.7 eV. These arguments in favor of our assignment of the two bands illustrate, we believe, further understanding of the complex nature of the band.

We shall now describe some considerations on the behavior of the E^{CT} in Y_2O_3:Eu^{3+} versus concentration as depicted in Figs. 2 and 4. In doing so, we shall concentrate on the E^{CT-2} curve in Fig. 4, because that curve is the most reliable.

For the discussion in the subsequent paragraphs we need the value of the lattice constant a of $(Y_{1-x}Eu_x)_2O_3$ as a function of the Eu^{3+} concentration. This constant was measured by Grill and Schieber,[32] who found a linear relationship between a and the Eu^{3+} concentration in the range of 0 to 100 Mol % Eu^{3+} in micrometer sized Y_2O_3:Eu^{3+}. For pure cubic Y_2O_3 $a = 1060.2$ pm and for pure cubic Eu_2O_3 $a = 1087$ pm.[32,33] The shortest distance d_{Ln-O} between Ln^{3+} (Ln^{3+} is Eu^{3+} or Y^{3+}) and O^{2-} can be approximated by:

$$d_{Ln-O} = \frac{a}{8}\sqrt{3}. \qquad [3]$$

In calculating d_{Ln-O} with Eq. 3 the small differences between the C_2 and C_{3i} sites in bixbyite $(Y_{1-x}Eu_x)_2O_3$[34,35] are neglected. It was found that an Y^{3+} ion at a C_2 site is not located at the ideal fluorite position, but rather 3.2 pm off-center,[34] whereas Y^{3+} at a C_{3i} site is in the center of the slightly distorted cube consisting of six O^{2-} ions and two diagonally opposed vacancies. If these small perturbations are neglected, d_{Y-O} is found to be 229.5 pm and d_{Eu-O} is 235.3 pm; the difference is 5.8 pm. The crystal ionic radii of Y^{3+} and Eu^{3+} are 104 pm and 108.7 pm ("crystal" radii, based on a radius of 126 pm for O^{2-}) respectively,[36] the difference amounts 4.7 pm. In other words the actual dilation of the lattice upon inserting more and more Eu^{3+} is a little bit larger than one would expect using the tabulated radii of the Eu^{3+} and Y^{3+} ions.

In the following text we shall, beside a purely electrostatic model, also briefly discuss Jørgensen's model of optical electronegativity, Kronig-Penney's model of the bandgap and an alternative bandgap-narrowing mechanism.

Electrostatic model.—Dorenbos[17] has tabulated the E^{CT} for various cubic Ln_2O_3:Eu^{3+} (where Ln = La, Gd, Y, Lu and Sc). For Y_2O_3:Eu^{3+} and Gd_2O_3:Eu^{3+} he mentioned 5.12 eV and 4.77 eV respectively. The ionic radii of Gd^{3+} and Eu^{3+} are 107.8 pm and 108.7 pm respectively. From the chemical kinship and the size similarity between Gd^{3+} and Eu^{3+} one expects that ΔE^{CT} between Y_2O_3:Eu^{3+} and Gd_2O_3:Eu^{3+} on the one hand and between Y_2O_3:Eu^{3+} and Eu_2O_3 on the other hand are almost equal. For the first pair Dorenbos indicated that $\Delta E^{CT} = 0.35$ eV and for the second pair, Y_2O_3:Eu^{3+} and Eu_2O_3, we found 0.41 eV (1% Y_2O_3: Eu^{3+}), which is indeed quite close. Dorenbos[17] and Blasse before him, based on other phosphor data,[12] assumed that the differences between E^{CT} of the cubic Ln_2O_3:Eu^{3+} with the large Ln^{3+} ionic radii may be explained by the Madelung energy. Let's investigate this hypothesis in somewhat more detail. The Madelung energy E_{Ma} of an ionic lanthanide oxide Ln_2O_3 can be written as:[37]

$$E_{Ma} = -1.44\frac{M_{Ln_2O_3}}{d_{Ln-O}}, \qquad [4]$$

where $M_{Ln_2O_3}$ is the Madelung constant for the molecule Ln_2O_3 in the cubic bixbyite lattice and d_{Ln-O} has been defined earlier. When d_{Ln-O} is expressed in nm, E_{Ma} is given in eV. The Madelung constant for cubic bixbyite-like Ln_2O_3 is 25.118.[34,38] In Fig. 9 we have represented E_{Ma} for the cubic Ln_2O_3 series together with data of Morss[37] and Jenkins and Roobottom[36] for the lattice (cohesion) energy and d_{Ln-O}.[38] The lattice energies will be discussed hereafter.

Fig. 9 shows that ΔE_{Ma} between Y_2O_3 and Eu_2O_3 is 3.74 eV and ΔE_{Ma} between Y_2O_3 and Gd_2O_3 is 3.06 eV: these differences are about a factor of 10 larger than the corresponding values for ΔE^{CT}
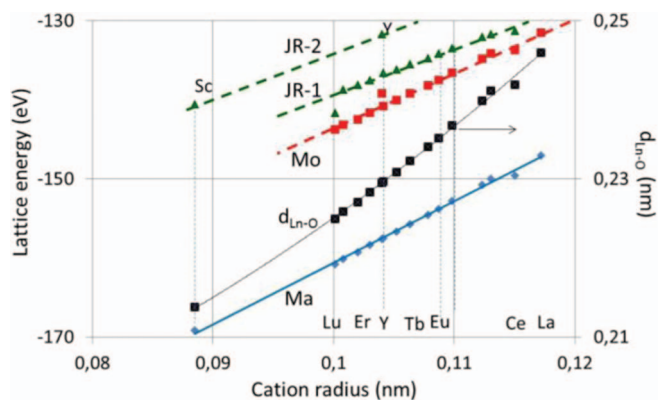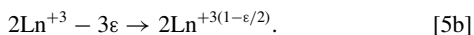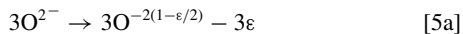

Figure 9. Lattice energy and Madelung energy of cubic (bixbyite) Ln_2O_3. Ma: Madelung energy, d_{Ln-O} is shortest Ln-O distance in the lattice (right hand vertical axis), Mo: lattice energy according to Morss,[36] JR-1 and JR-l: lattice energy according to Jenkins and Roobottom.[36]

mentioned above; in other words, the total Madelung energy of the compound is obviously not the right quantity to compare with the E^{CT}.

Let us consider what happens during charge transfer: during the charge rearrangement a small amount of charge ε (in units of the electron charge) located at an O^{2-} anion is transferred to an Ln^{3+} cation according to:

$$3O^{2-} \rightarrow 3O^{-2(1-\varepsilon/2)} - 3\varepsilon \qquad [5a]$$

$$2Ln^{+3} - 3\varepsilon \rightarrow 2Ln^{+3(1-\varepsilon/2)}. \qquad [5b]$$

The charge transfer during excitation of a photon can thus be represented by the following reaction:

$$Ln_2O_3 + h\nu \rightarrow 3O^{-2(1-\varepsilon/2)} + 2Ln^{+3(1-\varepsilon/2)} + 3\varepsilon\,(h+e), \qquad [6]$$

where the symbols e and h refer to an electron and hole respectively. According to Eq. 6 the charge transfer can be represented by the insertion of 3ε electron-hole (eh) pairs. Since ε is a small number, only a fraction of an eh-pair is inserted upon charge transfer. Eq. 6 implies that the Madelung energy of the insertion of 3ε eh-pairs needs to be evaluated, in which a fraction of the electron is positioned at the Ln^{3+} site and a (smaller) fraction of the hole at the O^{2-} site. The Madelung constant $M_{Ln_2O_3}$ represented in Eq. 4 is composed of two terms:

$$M_{Ln_2O_3} = 2z_{Ln}M_{Ln} + 3z_OM_O, \qquad [7]$$

where z_{Ln} and z_O are the ionic charges of the Ln^{3+} and O^{2-} ions, M_{Ln} and M_O are the Madelung constants for the cation and anion respectively and the numbers 2 and 3 represent the stoichiometric composition of Ln_2O_3. When 3ε eh-pairs per molecule Ln_2O_3 are introduced, then the Madelung constant M_{eh} of this insertion can be written as:

$$M_{eh} = z_eM_{Ln}\frac{\varepsilon}{2} + z_hM_O\frac{\varepsilon}{2} = -\frac{\varepsilon}{2}M_{Ln_2O_3} = -25.118\frac{\varepsilon}{2}, \qquad [8]$$

where $z_e = -1$ and $z_h = +1$. By exchanging $M_{Ln_2O_3}$ for M_{eh} in Eq. 4 the Madelung energy of the eh-pair fraction can be expressed as a function of the parameter ε. This energy is positive, because it requires energy to insert an electron at an Y^{3+} site and a hole at an O^{2-} site.

Fig. 10a shows the experimental E^{CT} and calculated ΔEM_{eh} curves as a function of Eu^{3+} concentration, where ΔEM_{eh} is defined as $EM_{eh}(x)-EM_{eh}(x=0.01)$. The ΔEM_{eh} curve shown in Fig. 10a refers to $\varepsilon = 0.33$, which means that the charge transfer in $(Y_{1-x}Eu_x)_2O_3$ can be represented by the insertion of one eh-pair per molecule Ln_2O_3 according to Eq. 6.

In Fig. 10b ΔEM_{eh} is compared with the E^{CT} of other cubic $Ln_2O_3:Eu^{3+}$ phosphors, the experimental E^{CT-D} for Lu, Y, Gd and La are from Dorenbos[17] while additional data for Y and Eu are from the present investigation. For the calculation of ΔEM_{eh} d_{Eu-O} is set to 229.5 pm for $Y_2O_3:Eu\rightarrow0$ and 235.3 pm for Eu_2O_3 as indicated afore. Although d_{Eu-O} is in the denominator of Eq. 4, the difference between the d_{Ln-O} values for $(Y_{1-x}Eu_x)_2O_3$ is so small that (almost) a straight line is obtained for ΔEM_{eh}, when plotted against the Eu^{3+} concentration. The same is valid for Fig 10b, in which ΔEM_{eh} has been plotted against the Ln^{3+} radius: the differences between d_{Ln-O} are still limited. Note that the vertical shifts of the ΔEM_{eh} lines in Figures 10a and 10b are slightly different. For $Lu_2O_3:Eu^{3+}$, $Y_2O_3:Eu^{3+}$, $Gd_2O_3:Eu^{3+}$ and Eu_2O_3, there is also a good agreement between ΔEM_{eh} and the E^{CT}. However, there is no agreement for $La_2O_3:Eu^{3+}$ and $Sc_2O_3:Eu^{3+}$[17] (not shown in Figure 10b). In the case of $La_2O_3:Eu^{3+}$ one cannot expect good agreement, because this material does not have a cubic bixbyite-like structure. We have no explanation why ΔEM_{eh} and the E^{CT} do not fit for $Sc_2O_3:Eu^{3+}$; an explanation might be sought in the deviating compressibility, which will be discussed briefly in the next paragraph. Nevertheless, from the considerations described here, we conclude that the variation of the E^{CT} in $(Y_{1-x}Eu_x)_2O_3$ as a function of the Eu^{3+} concentration is primarily caused by the change of the electrostatic energy upon inserting an eh-pair into the lattice.
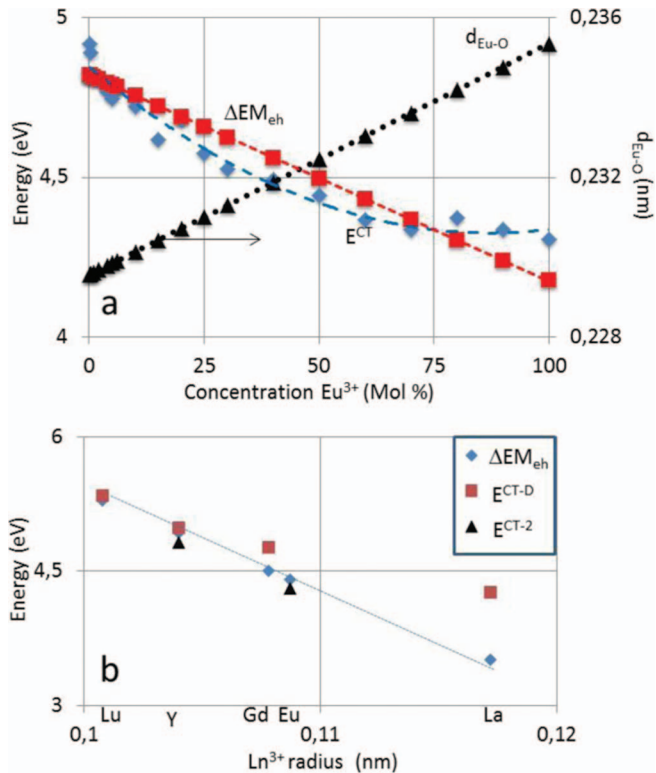

Figure 10. E^{CT}, ΔEM_{eh} and d_{Eu-O} (right hand scale) as a function of Eu^{3+} concentration for $(Y_{1-x}Eu_x)_2O_3$ in (a) ΔEM_{eh} and E^{CT} for $Lu_2O_3:Eu^{3+}$, $Y_2O_3:Eu^{3+}$, $Gd_2O_3:Eu^{3+}$, Eu_2O_3 and $La_2O_3:Eu^{3+}$ versus Ln^{3+} radius in (b) E^{CT-D} are data from Dorenbos,[17] E^{CT-2} are data from Figure 4.

In recent papers Dorenbos has introduced the concept of chemical shift,[39,40] which is the coulomb interaction between a 4f electron near the Eu nucleus and the total charge of Eu^{3+} that is located at a distance R_Q from that nucleus. This chemical shift E(shift) can be written as:

$$E(shift) = -1.44\frac{Q}{R_Q}, \qquad [9]$$

where Q = 3, represents the total charge of the trivalent Eu ion. The distance R_Q, called the screening distance, expressed in nm when E(shift) is expressed in eV, is a parameter that varies from compound to compound.[39] The similarity between Eq. 4 and Eq. 9 is striking: when the E(shift) is applied to E^{CT}-data, it indicates that the ratios $3/R_Q$ (in Eq. 9) and $\varepsilon M_{Ln_2O_3}/(2d_{Ln_2O_3})$ (after combining Eqs. 4 and 8) represent the same behavior. The difference is that the charge ε in Eq. 8 needs to be fitted to the experimental data, whereas R_Q in Eq. 9 is the parameter to be fitted. Table I shows a comparison between the Madelung and chemical shift methods for the data presented here. This comparison is based on the value of ΔEM_{eh} calculated with the Madelung energy method shown in Fig. 10a, which slightly overestimates the experimental value of ΔE^{CT}.

When R_Q of 100% Eu_2O_3 is chosen to be 0.193 nm, as suggested by Dorenbos,[39] a value of R_Q for $Y_2O_3:Eu^{3+}$ with 1% Mol Eu^{3+} of

Table I. Comparison Madelung and Chemical Shift Methods for E^{CT} of $(Y_{1-x}Eu_x)_2O_3$.

	ΔE^{CT}(eV) (calc.)	d_{Ln-O}(Eu) (nm)	d_{Ln-O}(Y) (nm)	R_Q(Eu) (nm)	R_Q(Y) (nm)
ΔEM_{eh}	0.62*	0.2351	0.2295		
$\Delta E(shift)$	0.62			0.193	0.1878

*ΔEM_{eh} refers to the Madelung constant of Eq. 8 with $\varepsilon = 0.33$.

0.1878 nm yields $\Delta E(shift) = \Delta E^{CT} = 0.62$ eV. The difference between R_Q for Eu_2O_3 and 1% $Y_2O_3:Eu^{3+}$ is 5.2 nm, which is almost equal to the difference between the radii of Eu^{3+} and Y^{3+}, indicating that R_Q varies with $r_{Ln}{}^{3+}$. It should be mentioned that this comparison depends on the original choice for R_Q of Eu_2O_3; however, in the plausible range of R_Q–values indicated by Dorenbos,[39] this comparison does not change significantly.

It is tempting to speculate about the (small) differences between the experimental E^{CT} and the ΔEM_{eh} curves in Fig. 10a. For this speculation we shall make use of Fig. 9, in which both lattice energies and Madelung energies of the cubic Ln_2O_3 (including Y_2O_3 and Sc_2O_3) crystals have been plotted. Four lines are represented in Fig. 9: Ma stands for the Madelung energies of the Ln_2O_3 crystals, Mo stands for the lattice energies as tabulated by Morss,[37] the lines JR-1 and JR-2 are based on the lattice energies from Jenkins and Roobottom, tabulated in the Handbook of Chemistry and Physics.[36] The lattice energies represented in Fig. 9 were calculated with the Born-Haber cycle from thermodynamic data or were estimated with Born-Landé's equation. Fig. 9 shows that the Madelung energy of the Ln_2O_3 series overestimates the (absolute value of the) lattice energy by about 8%. The difference between lattice energy and Madelung energy is usually ascribed to the effect of polarizability of the ions. If we would have based the calculation of ΔEM_{eh} in Fig. 10a on lattice energy instead of Madelung energy, the slope of the ΔE_{e-h} line would be 8% less steep. However, the increasing effect of the polarizability of the cation by inserting more and more Eu^{3+} in the lattice might well lead to a deviation from linearity as shown by the E^{CT}-curve. The JR-2 line in Fig 9 suggests that polarizability effects in Y_2O_3 and Sc_2O_3 are larger than in the Ln_2O_3 series, which is gainsaying the reasoning given above. However, beside the difference in polarizability between the Y^{3+} and Eu^{3+} ions, another effect has to be taken into account: compressibility as known from Born-Landé's equation. Both Y^{3+} and Sc^{3+} are rather small ions, these may create, even after adjustment of the lattice constant, slightly more space for compression leading to a smaller Born exponent. This argument largely eliminates the contradiction mentioned here.

Non-electrostatic models.—In this section some non-electrostatic models will briefly be considered that could explain the behavior of the E^{CT} shown in Figs. 2 and 4. First Jørgensen's model of optical electronegativity will be discussed. As suggested by Krumpel et al.,[18] the optical electronegativity of Eu^{3+} in Eu^{3+} doped phosphors may be represented by a function of $(d_{C-O})^{-1}$, where the subscript C represents the central ion in the lattice that may be replaced by Eu^{3+}. In view of the small difference between the values d_{Y-O} in Y_2O_3 and d_{Eu-O} in Eu_2O_3, the optical electronegativity of Eu^{3+} may also be described by a linear function of the d_{Ln-O} distance in $(Y_{1-x}Eu_x)_2O_3$. In doing so, the experimental E^{CT} curve can be fitted with a straight line, which is determined by two parameters p and q in the relation $\chi(Eu) = p + qd_{Ln-O}$. Since the physical interpretation of these parameters is not straightforward, we do not consider this treatment as appropriate for explaining the redshift of the CT-band in $Y_2O_3:Eu^{3+}$.

The second model to be discussed is the Kronig-Penney model[41] of the bandgap of a semiconductor, which has been applied to $Y_2O_3:Eu^{3+}$ nanocrystals by Shang et al.[9] According to these authors the change of the bandgap energy ΔE_g can be written as:

$$\Delta E_g = -\frac{2}{3}E_g\frac{\Delta v}{v}, \qquad [10]$$

where Eg is the bandgap of Y_2O_3 (or $Y_2O_3:Eu^{3+}$ with a very small Eu^{3+} concentration), Δv is the change of volume of a unit cell upon Eu^{3+} doping and v is the volume of the cell for non-doped Y_2O_3. Shang et al. dealt with dilation of the lattice upon reducing the particle size, whereas we dealt with lattice dilation upon increasing the dopant concentration, which is different.

In going from Y_2O_3 to Eu_2O_3 the cell constant changes by 2.52% and the cell volume by 7.78%. When inserting this value for $\Delta v/v$ in Eq. 10 and taking a value of 5.6 eV for the bandgap of 1% $Y_2O_3:Eu^{3+}$[42] we get $\Delta E_g = 0.29$ eV, which is lower than ΔE^{CT}, being 0.41 eV

in going from 1% $Y_2O_3:Eu^{3+}$ to 100% Eu_2O_3. When plotting ΔE_g versus Eu^{3+} concentration one gets a straight line, because the small change of the lattice constant leads to a linear change of Δv versus Eu^{3+} concentration. Notwithstanding the 67% agreement between the Kronig-Penney model for ΔE_g and the E^{CT}, which is surprisingly good, we discard the Kronig-Penney model because apart from the lattice constant a, the wave functions of the Ln^{3+} ion are also changing upon doping. Furthermore, one should keep in mind that, because of the effect of the photo-ionization (or photo-conductivity) threshold defined in Eq. 2, a good agreement between ΔE_g and $\Delta v/v$ does not guarantee a good correlation between the ΔE^{CT} and $\Delta v/v$.

As a third possibility we now consider a bandgap-narrowing model that was developed in the 1970s for heavily doped Si and Ge. This model was applied to the semi-insulator GaAs by Hrivnák.[43] The equation describing this type of bandgap-narrowing can be written as:

$$\Delta E_g(N) = -17.55\sqrt{\frac{N}{10^{18}cm^{-3}}}, \qquad [11]$$

where ΔEg is the bandgap-narrowing (in eV) and N is the dopant concentration in atoms/cm^3. For the calculation of the constant 17.55 we used a dielectric constant of 15 for Y_2O_3. By inserting the Eu^{3+} concentrations in Eq. 11 as used in our experiments, ΔEg is about one order of magnitude larger than ΔE^{CT}. For this reason this model can be discarded as well.

Finally we must consider spin-spin interaction between the Eu^{3+} ions in the lattice. Eu^{3+} is a high spin ion, because the six 4f electrons are parallel oriented. The cubic lanthanide sesquioxides including Eu_2O_3 are antiferromagnetic at low temperatures. The reported Néel temperatures for all Ln_2O_3 are <10 K,[44] which means that the energy for magnetic ordering is <0.9 meV. In other words, spin-spin interactions between Eu^{3+} ions at neighboring sites in $(Y_{1-x}Eu_x)_2O_3$ have a very small effect on the energy levels and may be neglected here.

Conclusions

We have found that the CT-band in $(Y_{1-x}Eu_x)_2O_3$ has a substantial redshift upon increasing the Eu^{3+} concentration. The redshift amounts 0.43 eV in going from 0.1 Mol % Eu^{3+} to 100%. We have established herein that the CT-band consists of two sub-bands, both of which show equal redshift. Evidence is presented herein that these two bands are directly related to the two symmetry sites for the Ln^{3+} ion in the cubic bixbyite type lattice of $(Y_{1-x}Eu_x)_2O_3$. The redshift of this CT-band can quantitatively be described in terms of the Madelung energy of one inserted eh-pair. The E^{CT} of some $Ln_2O_3:Eu^{3+}$ phosphors with radii of the Ln^{3+} cation that do not deviate much from those of Y^{3+} and Eu^{3+} (Gd^{3+} and Lu^{3+}) can be described with this electrostatic model.

We suggest that the electrostatic analysis presented in our study could help to improve the understanding of the variation of the E^{CT} in some of the phosphors studied and classified by Dorenbos[39] by unifying his chemical shift model with the Madelung energy model. In addition as we have shown that the CT band is made up of contributions from both lattice sites it may be possible to make more detailed inferences to further the understanding of the CT bands of lattices containing more than two different lattice sites.

References

1. L. Ozawa, *Cathodoluminescence, Theory and Applications*, Kodansha & VCH Verlag, Tokyo, 1990, Chapter 8, 165.
2. V. Pelova, K. Kynev, T. Petrova, and Tz. Piperov, *Cryst. Res. Technol.*, **33**, 125 (1998).

3. H. Chang, I. W. Lenggoro, K. Okuyama, and T. O. Kim, *Jpn. J. Appl. Phys.*, **43**, 3535 (2004).
4. C. Hang, Z. P. Fen, Z. H. Yang, L. H. Dong, and C. Q. Liang, *Chin. Phys. B*, **23**, 057801 (2014).
5. Y. C. Kang, S. B. Park, I. W. Lenggoro, and K. Okuyama, *J. Mater. Res.*, **14**, 2611 (1999).
6. T. Igarashi, M. Ihara, T. Kusunoki, K. Ohno, T. Isobe, and M. Senna, *Appl. Phys. Lett.*, **76**, 1549 (2000).
7. Z. Fu, S. Zhou, T. Pan, and S. Zhang, *J. Lumin.*, **124**, 213 (2007).
8. M. Jia, J. Zhang, S. Lu, J. Sun, Y. Luo, X. Ren, H. Song, and X. J. Wan, *Chem. Phys. Lett.*, **384**, 193 (2004).
9. C. Y. Shang, X. Q. Wang, H. Kang, and D. M. Han, *J. Appl. Phys.*, **109**, 104309 (2011).
10. W. W. Zhang, W. P. Zhang, P. B. Xie, M. Yin, H. T. Chen, L. Jing, Y. S. Zhang, L. R. Lou, and S. D. Xia, *J. Colloid Interface Sci.*, **262**, 588 (2003).
11. L. E. Brus, *J. Chem Phys.*, **80**, 4403 (1984).
12. G. Blasse, *J. Chem. Phys.*, **45**, 2356 (1996).
13. H. E. Hoefdraad, *J. Solid State Chem.*, **15**, 175 (1975).
14. C. K. Jørgensen, *Modern Aspects of Ligand Field Theory*, North-Holland Publishing Company, Amsterdam, 1971.
15. L. van Pieterson, M. Heeroma, E. de Heer, and A. Meijerink, *J. Lumin.*, **91**, 177 (2000).
16. P. Dorenbos, *J. Phys.: Condens. Matter*, **15**, 8417 (2003).
17. P. Dorenbos, *J. Lumin.*, **111**, 89 (2005).
18. A. H. Krumpel, P. Boutinaud, E. van der Kolk, and P. Dorenbos, *J. Lumin.*, **130**, 1357 (2010).
19. W. C. Wong, D. S. McClure, S. A. Baun, and M. R. Kokta, *Phys. Rev.*, **B 51**, **5682**, (1995).
20. J. B. Prasanna kumar, G. Ramgopal, Y. S. Vidya, K. S. Anantharaju, B. Daruka Prasad, S. C. Sharma, S. C. Prashantha, H. B. Premkumar, and H. Nagabhushana, *Spectrochim. Acta Part A: Mol. Biomol. Spectrosc.*, **141**, 149 (2015).
21. D. den Engelsen, P. G. Harris, T. G. Ireland, G. Fern, and J. Silver, *ECS J. Solid State Sci. Technol.*, **4**, R145 (2015).
22. D. den Engelsen, P. G. Harris, T. G. Ireland, and J. Silver, *ECS J. Solid State Sci. Technol.*, **4**, R1, (2015).
23. D. den Engelsen, P. G. Harris, T. G. Ireland, R. Withnall, and J. Silver, *ECS J. Solid State Sci. Technol.*, **2**, R201 (2013).
24. X. Jing, T. Ireland, C. Gibbons, D. J. Barber, J. Silver, A. Vecht, G. Fern, P. Trogwa, and D. C. Morton, *J. Electrochem. Soc.*, **146**, 4654 (1999).
25. J. Silver, T. G. Ireland, and R. Withnall, *J. Electrochem. Soc.*, **151**, H66 (2004).
26. R. B. Hunt Jr. and R. G. Pappalardo, *J. Lumin.*, **34**, 133 (1985).
27. L. Ozawa, *Jpn. J. Appl. Phys.*, **5**, 740 (1996).
28. M. Buijs, A. Meyerink, and G. Blasse, *J. Lumin.*, **37**, 9 (1987).
29. D. B. M. Klaassen, R. A. M. van Ham, and T. G. M. van Rijn, *J. Lumin.*, **43**, 261 (1989).
30. R. G. Pappalardo and R. B. Hunt Jr., *J. Electrochem. Soc.*, **132**, 721 (1985).
31. D. den Engelsen, P. G. Harris, T. G. Ireland, G. Fern, and J. Silver, *ECS J. Solid State Sci. Technol.*, **4**, R105 (2015).
32. A. Grill and M. Schieber, *Phys. Rev. B*, **1**, 2241 (1970).
33. L. Robindro Singh, R. S. Ningthoujam, V. Sudarsan, I. Srivastava, S. Dorendrajit Singh, G. K. Dey, and S. K. Kulshreshtha, *Nanotechnol.*, **19**, 055201 (2008).
34. H. E. v. Mertens and J. Zemann, *Acta Cryst.*, **21**, 467 (1966).
35. K. Endo, S. Yamauchi, K. Fueki, and T. Mukaibo, *Bull. Chem. Soc. Jpn.*, **49**, 1191 (1976).
36. *Handbook of Chemistry and Physics*, Ed. D. R. Lide, 84th Edition, CRC Press, 2003.
37. L. R. Morss, *Chem. Rev.*, **76**, 827 (1976).
38. B. M. Angelov, *J. Phys. C: Solid State Phys.*, **15**, L239 (1982).
39. P. Dorenbos, *Phys. Rev. B*, **85**, 165107, (2012).
40. P. Dorenbos, *ECS J. Solid State Sci. Technol.*, **2**, R3001 (2013).
41. A. Many, Y. Goldstein, and N. B. Grover, *Semiconductor Surfaces*, North-Holland Publishing Company, Amsterdam, 1965.
42. W. C. Wang, M. Badylevich, V. V. Afanas'ev, A. Stesmans, C. Adelmann, S. Van Elshocht, J. A. Kittl, M. Lukosius, Ch. Walzcyk, and Ch. Wenger, *Appl. Phys. Lett.*, **95**, 132903 (2009).
43. L. Hrivnák, *J. Appl. Phys.* **62**, 3228 (1987).
44. S. Kern and R. Kostelecky, *J. Appl. Phys.*, **42**, 1773 (1971).